

Three-Dimensional Digital Topological Characterization of Cancellous Bone Architecture

Punam K. Saha,¹ Bryon R. Gomberg,² Felix W. Wehrli³

¹ Medical Image Processing Group, Department of Radiology, University of Pennsylvania, Philadelphia, PA 19104

² Department of Bioengineering, University of Pennsylvania, Philadelphia, PA 19104

³ Laboratory for Structural NMR, Department of Radiology, University of Pennsylvania, 3400 Spruce Street, Philadelphia, PA 19104. E-mail: wehrli@oasis.rad.upenn.edu

ABSTRACT: Cancellous bone consists of a network of bony struts and plates that provide mechanical strength to much of the skeleton at minimum weight. It has been shown that loss in bone mass is accompanied by architectural changes that relate to both scale and topology of the network. In this paper, the concept of three-dimensional (3D) digital topology is presented for characterizing the local topology of each bone voxel after skeletonization of the binary bone images. This method allows us to identify each voxel as belonging to a surface, curve, or junction structure in the trabecular bone network. The method has been quantitatively validated on synthetic images demonstrating its relative immunity to partial volume blurring and noise. Parameters introduced to characterize network topology include surface-to-curve ratio and erosion index. Finally, the technique is shown to quantify the architecture of human trabecular bone in magnetic resonance micro-images acquired from cadavers and *in vivo*. © 2000 John Wiley & Sons, Inc. *Int J Imaging Syst Technol*, 11, 81–90, 2000

I. INTRODUCTION

Trabecular (also denoted cancellous) bone, which makes up most of the axial skeleton and the ends near the joints of the long bones, consists of a lattice of plates and struts. This organization provides mechanical strength to the skeleton at minimum weight. It is widely accepted that the mechanical competence of trabecular bone (i.e., its resistance to fracturing) is a function of both mass density and architecture and that disease processes such as osteoporosis entail both loss in net bone mass and architectural deterioration (World Health Organization [WHO], 1994). Quantification of the structural make-up of trabecular bone is therefore of paramount interest.

Most studies concerned with the quantitative description of trabecular bone have used histomorphometry from sections in conjunction with stereology (Parfitt, 1981) to reconstruct the third dimension. Recent advances in micro-imaging technology, notably micro-computed tomography (μ -CT; Müller et al., 1994) and magnetic resonance imaging (MRI; Wehrli, 1998), make it possible to image

trabecular bone *in vitro* in cadaveric specimens or bone biopsies, and more recently *in vivo*, and to analyze the resulting images using digital image processing (Hwang and Wehrli, 1999).

Trabecular bone strength is related to thickness, number density, and orientation of the trabeculae. Gordon et al. measured such quantities as connectivity, hole size, and structural orientation from skeletonized two-dimensional (2D) CT (1996) and MR images (1997) *in vivo*. They demonstrated that these parameters change characteristically with subject age. Feldkamp et al. (1989) used topological arguments to describe trabecular lattices by measuring connectivity, expressed in terms of the global Euler characteristic, from 3D images obtained by μ -CT. The Euler characteristic, derived from the Euler-Poincaré formula, assumes the number of bone objects to be one and that marrow cavities do not exist in the network. These assumptions make the Euler characteristics equivalent to the first Betti number (Feldkamp et al., 1989), a measure of the number of loops in the network. This approach has been successful in characterizing osteoporotic changes in laboratory animals, demonstrating that the reduction in connectivity following bone loss and recovery parallels the reduction in Young's modulus for loading (Kinney and Ladd, 1998). However, the method has its limitations. For example, the first Betti number is inherently insensitive to trabecular erosion, which is known to result in perforation of trabecular bone plates and disconnection of rodlike trabecular bone (Amling et al., 1996; Parfitt, 1992). Therefore, the first Betti number will decrease from loss of rods, causing a reduction in the number of loops. However, it would increase as a result of perforation of plates, which increases the number of loops. Therefore, the first Betti number would not necessarily detect osteoporotic bone erosion.

The strength of trabecular lattices is determined by three categories of parameters relating to the bone's material, scale, and topological properties (deHoff et al., 1972). Material properties describe the bone material, scale properties, and the size and spacing of the trabecular elements; topology describes the arrangement of the bone in the network. Osteoporosis is characterized as a disorder resulting from bone erosion (WHO, 1994) where the bone's intrinsic material properties are often assumed to be invariant. Bone erosion causes changes in the scale and topology of the trabecular network.

Correspondence to: Felix W. Wehrli

Contract grant sponsor: NIH, Contract grant numbers: R0141443, NS37172; Contract grant sponsor: Department of the Army; Contract grant number: DAMD 179717271.

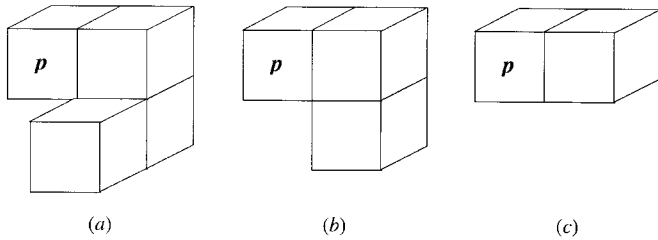


Figure 1. Examples of 26-, 18-, and 6-adjacencies (shown in (a), (b), and (c), respectively) in a cubic grid.

Scale properties include such parameters as trabecular bone thickness and volume fraction.

In the present work, we introduce a method that allows the unequivocal determination of the topological class pertaining to each bone voxel of the 3D trabecular network. The method is based on determining the connectivity of the neighbors in the $3 \times 3 \times 3$ neighborhood (Saha and Chaudhuri, 1996) of the voxel examined. The starting point of the analysis is the conversion of the 3D network to a skeletonized surface representation, which contains only 1D and 2D structures only (i.e., curves and surfaces). The voxels are then assigned to the appropriate topological class (e.g., curves, surfaces, or junctions) in a three-step approach. This method is validated on synthetic images and illustrated with selected MR images of trabecular bone, obtained in two resolution regimens: (1) in cadaveric specimens and (2) *in vivo*. Finally, we show that the topological quantities parallel the visual appearance of the structures.

II. THEORY

The basis of digital topological classification relies on determining the local topological parameters—the numbers of objects, tunnels, and cavities—in the immediate neighborhood of a bone voxel. In this section, we present the concepts of digital topological analysis in the context of trabecular bone images. Digital topology deals with binary images defined as 3D arrays of voxels whose positions are represented by Cartesian coordinates (x_1, x_2, x_3) and whose voxels can only have two values (bone or marrow). Such images are usually obtained by binarizing a gray-scale intensity image, such as thresholding a bone volume fraction (BVF) image. Two voxels (x_1, x_2, x_3) and (y_1, y_2, y_3) are called 6-adjacent if $\sum_{i=1}^3 (x_i - y_i)^2 = 1$ (face adjacent only); they are called 18-adjacent if $\sum_{i=1}^3 (x_i - y_i)^2 \leq 2$ (face and edge adjacent); and they are called 26-adjacent if $\sum_{i=1}^3 (x_i - y_i)^2 \leq 3$ (face, edge, and corner adjacent). Figure 1 gives examples of each of these adjacencies. Let S be a nonempty set of voxels, such as all the bone voxels in a 3D digital image. An α -path (where α can be 6, 18, or 26) between two voxels $p, q \in S$ means a sequence of voxels p_0, p_1, \dots, p_n ($p = p_0$ and $q = p_n$) in S such that p_i is α -adjacent to p_{i+1} , $0 \leq i < n$. An α -path is an α -closed path if p_0 is α -adjacent to p_n . Two voxels $p, q \in S$ are α -connected in S if there exists an α -path from p to q in S . An α -object of S is a maximal subset of S where each pair of voxels is α -connected. A set of voxels is simply connected if it is connected and contains no tunnel.

Bone objects are defined as 26-objects of bone voxels (i.e., 26-connected) and marrow objects (background) are 6-objects of marrow voxels. To satisfy the Jordan surface property in a binary image, whenever 26-connectivity is used for foreground (i.e., the set of bone voxels), 6-connectivity must be used for the background

(i.e., the set of marrow voxels; Rosenfeld, 1974). This ensures that a closed bone surface will separate the background into two marrow objects, the interior and the exterior. If the marrow had greater than 6-connectivity and the bone voxels formed a diagonal surface, the supposedly disconnected interior and exterior marrow objects would be connected by corner or edge adjacency across the bone surface. This situation contradicts the fundamental topological behavior of simple closed surfaces, and hence is not acceptable. Thus, bone objects are determined by face, edge, or corner voxel adjacency; marrow objects are only determined by face adjacency.

A cavity is a marrow object surrounded by a bone object. Because the marrow space in trabecular bone is assumed to be connected, no such cavities exist in trabecular bone networks. However, as a part of the process of determining the connectivity in the local neighborhood, the central bone voxel is considered a marrow (background) voxel which, technically, can result in a single voxel cavity. For example, if three 6-connected orthogonal straight lines intersect at a single voxel, when that voxel is considered marrow, a cavity is formed.

Although tunnels are easily visualized and intuitively described, they are difficult to formally define. However, the number of tunnels in an object can be defined precisely. Intuitively, a tunnel would be the handle of a coffee mug, formed by bending a cylinder to connect the two ends to each other or to a single connected object. There exists a connection between tunnels and handles—when the coffee mug's handle is broken, the tunnel is lost. In most objects, the number of tunnels can be counted by recursively reducing the number of handles. If the object has a cavity that forms a handle (e.g., the interior of a hollow torus), this cavity must be filled first, and then the exterior handles counted. For example, a ring has one tunnel because the object forms a single solid handle. A hollow torus has two tunnels: the first arises from the cavity inside the ring and the second from the ring itself. A handle is an object that can be elastically deformed to a simple, closed curve. More accurately, the number of tunnels in an object is the rank of its first homology group (Kong and Rosenfeld, 1989). The number of objects, tunnels, and cavities represent the 0^{th} , 1^{st} , and 2^{nd} Betti numbers, respectively.

In the following discussions, for any bone voxel p , $N(p)$ denotes the set of 27 voxels in the $3 \times 3 \times 3$ neighborhood of p (including the central voxel p) and $N^*(p)$ denotes the set of 26 voxels in the $3 \times 3 \times 3$ neighborhood of p (excluding p , i.e., p is considered marrow). Because the bone structure of $N(p)$ always contains exactly one simply connected object without cavities (Saha and Rosenfeld, 1998), the topological properties of $N(p)$ are invariant and $N^*(p)$ must be used to characterize the local topology. Let $\xi(p)$, $\eta(p)$, and $\delta(p)$, respectively, denote the number of objects, tunnels, and cavities in the bone structure of $N^*(p)$. We call $\xi(p)$, $\eta(p)$, and $\delta(p)$ local topological parameters of p . Let $X(p)$ and $Y(p)$ be the sets of 6- and 18-adjacent marrow voxels to p , respectively. It may be noted that a marrow object in $Y(p)$ can be either 6- or 18-adjacent to p , depending on whether or not it intersects $X(p)$. The following two theorems provide a computational definition of $\eta(p)$ and $\delta(p)$ in the bone structure of $N^*(p)$:

Theorem 1. *If $X(p)$ is nonempty, the number of tunnels, $\eta(p)$, is one less than the number of marrow objects of $Y(p)$ that intersects $X(p)$, or zero otherwise.*

Theorem 2. *The number of cavities, $\delta(p)$, is one when all the 6-neighbors of p are bone voxels and zero otherwise.*

Whereas Theorem 2 is trivial, Theorem 1 needs some clarification. In the continuous topological space, \mathcal{R}^3 , a topological sphere, $S_{\mathcal{R}^3}$, is any object that can be elastically deformed to the boundary of

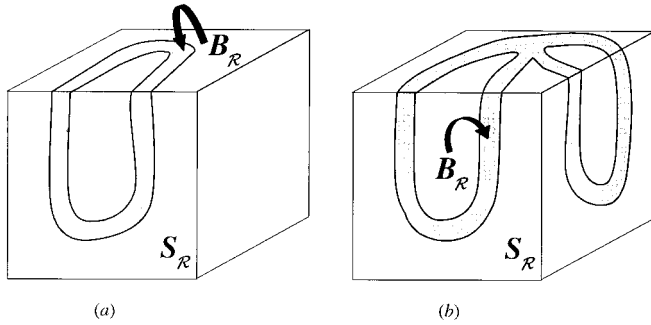


Figure 2. Examples of tunnels on the boundary of a topological ball. (a) $B_{\mathcal{R}}$ forms one tunnel and $S_{\mathcal{R}} - B_{\mathcal{R}}$ generates exactly two components. (b) $B_{\mathcal{R}}$ forms two tunnels and $S_{\mathcal{R}} - B_{\mathcal{R}}$ generates exactly three components.

a solid ball (e.g., the surface of a brick). Following the Jordan curve property, a subset, $B_{\mathcal{R}}$, of such a sphere forms a tunnel if $B_{\mathcal{R}}$ forms a loop and therefore disconnects $S_{\mathcal{R}}$ into several objects, i.e., $S_{\mathcal{R}} - B_{\mathcal{R}}$ has more than one object. If $S_{\mathcal{R}} - B_{\mathcal{R}}$ is empty, there is no tunnel; otherwise, the number of tunnels is one less than the number of objects in $S_{\mathcal{R}} - B_{\mathcal{R}}$. Figure 2 demonstrates the fact. In Figures 2(a) and (b), $B_{\mathcal{R}}$ forms 1 and 2 tunnels, respectively. It may be seen that, in Figures 2(a) and (b), $S_{\mathcal{R}} - B_{\mathcal{R}}$ has two and three objects, respectively. Returning to our problem in digital topology, our sphere is $N^*(p)$, and our subset, B (analogous to $B_{\mathcal{R}}$ in continuous space), is the set of bone voxels in $N^*(p)$. $N^*(p) - B$ is the set of marrow voxels on the digital sphere. The number of tunnels in $N^*(p)$ is, therefore, one less than the number of marrow objects in $N^*(p)$, after the following two important considerations.

The first consideration has to do with the marrow objects that can contribute a tunnel. To form a tunnel, the marrow object must be adjacent to the interior of the sphere (i.e., p in the digital space). Therefore, the marrow objects in $N^*(p)$ that are not 6-adjacent to p cannot contribute a tunnel and we must consider only the marrow objects that intersect $X(p)$. The second consideration is that the corners of $N^*(p)$ must be excluded from the set of marrow voxels to be able to apply the Jordan curve theorem on a digital sphere—a closed curve on a sphere must divide it into two objects. This means that a ring of bone voxels on $N^*(p)$ should always disconnect $N^*(p)$ into two objects. Consider the ring of bone voxels in Figure 3. Although these bone voxels form a loop, they do not disconnect the marrow “shell” into two marrow objects because a 6-path of marrow voxels (shown by arrow) exists between the two supposedly disconnected marrow objects (to left and right of the loop). The 6-path of marrow voxels crosses the loop of bone voxels on the digital closed surface of $N^*(p)$, creating an anomaly of the Jordan curve property in digital space. By excluding the corners of $N^*(p)$ from the marrow objects, we forbid marrow paths from crossing a loop of bone voxels and therefore from joining separate marrow objects (Fig. 3b). Therefore $Y(p)$ includes only the marrow voxels that are 18-adjacent to p . Rigorous proof of these theorems can be found in Saha and Rosenfeld (2000).

A. Efficient Computation. We describe an efficient method of computing $\xi(p)$, $\eta(p)$, and $\delta(p)$. A face of $N^*(p)$ is the set of 3×3 voxels, all being at the same side of $N^*(p)$. The unique 6-neighbor on a face of $N^*(p)$ will be referred to as the representative voxel of that face. Similarly, an edge of $N^*(p)$ is the set of three voxels, all

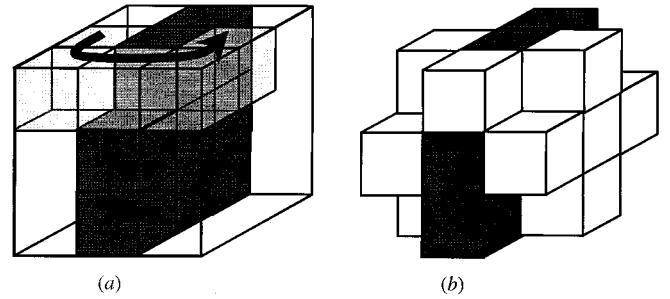


Figure 3. Example of tunnels on the boundary of a digital $3 \times 3 \times 3$ cube. Bone voxels are shown dark; marrow voxels are shown transparent and semitransparent in (a) and opaque in (b). In both (a) and (b), bone voxel configurations are the same. (a) shows that a marrow path (shown by semitransparent voxels) may cross a closed bone path on the boundary of a $3 \times 3 \times 3$ cube. (b) demonstrates $Y(p)$; note that no marrow path of $Y(p)$ crosses the closed bone path.

being at the intersection of two faces of $N^*(p)$. The unique 18-neighbor on an edge of $N^*(p)$ will be referred to as the representative voxel of that edge. A face and an edge of $N^*(p)$ along with their representative voxels are shown in Figure 4. The method of computing topological parameters is primarily built on the following theorem.

Theorem 3. When the representative voxel of a face or an edge is bone, the topological parameters $\xi(p)$, $\eta(p)$, and $\delta(p)$ are independent of the other voxels in that face or edge.

Rigorous proof of this theorem is published in Saha and Rosenfeld (2000). A face or an edge of $N^*(p)$ can be called dead if its representative voxel is a bone voxel. Otherwise, the voxels of that face or edge may contribute to the local topological parameters of $N^*(p)$. A voxel will be called effective if it does not lie on a dead face or edge. To determine $\xi(p)$, $\eta(p)$, and $\delta(p)$, it is sufficient to know the configuration of effective voxels. After determining the configuration of all 6-neighbors, the algorithm computes the topological parameters using a lookup table of effective voxel configurations. There are 64 possible configurations of 6-neighbors. However, these configurations can be grouped based on the relative positions of bone 6-neighbors. A geometric class of $N^*(p)$ is a set of all 6-neighbor configurations that are equivalent under orthogonal symmetry operations. The computations of topological parameters for all 6-neighbor configurations in the same geometric class are identical. There are 10 possible geometric classes in $N^*(p)$.

Class 0: All 6-neighbors are bone. Number of effective voxels $(n_e) = 0$.

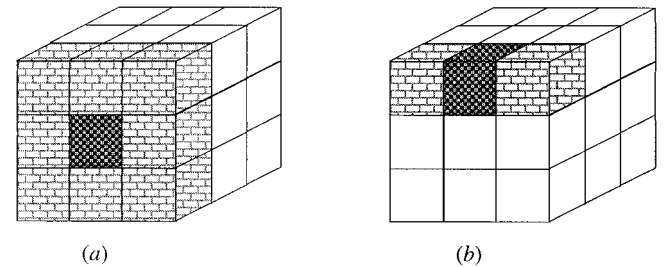


Figure 4. Demonstration of faces and edges of $N^*(p)$. Voxels on a face (a) or on an edge (b) are shown in gray pattern. The representative voxels are shown in dark gray pattern.

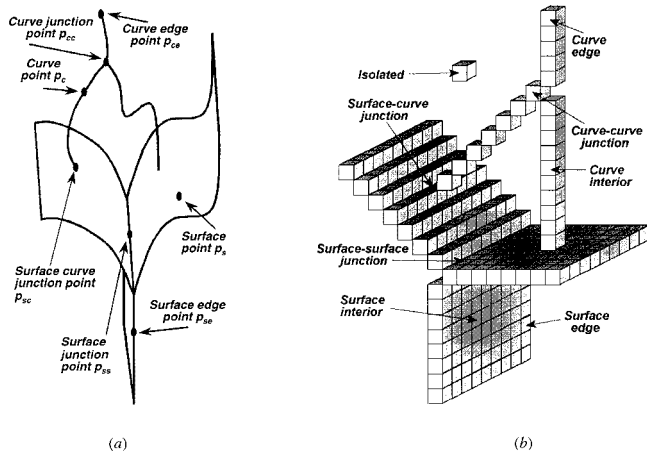


Figure 5. Illustration of possible topological classification in a surface and curve representation. (a) An example in continuous 3-space \mathcal{R}^3 . (b) An example in digital space.

- Class 1:** Five 6-neighbors are bone. $n_e = 0$.
- Class 2:** Two pairs of opposite 6-neighbors are bone. $n_e = 0$.
- Class 3:** One pair of opposite and two nonopposite 6-neighbors are bone. $n_e = 1$.
- Class 4:** One pair of opposite and another 6-neighbors are bone. $n_e = 2$.
- Class 5:** Three nonopposite 6-neighbors are bone. $n_e = 4$.
- Class 6:** One pair of opposite 6-neighbors is bone. $n_e = 4$.
- Class 7:** Two nonopposite 6-neighbors are bone. $n_e = 7$.
- Class 8:** Only one 6-neighbor is bone. $n_e = 12$.
- Class 9:** No 6-neighbor is bone. $n_e = 20$.

For geometric Classes 0–2, there is no effective voxel and the parameters are immediately known. For example, in Class 2, $\xi(p) = 1$, $\eta(p) = 1$, and $\delta(p) = 0$. Except for Class 9, there are only a few effective voxels. A straightforward lookup table can be used that provides the values of $\xi(p)$, $\eta(p)$, and $\delta(p)$ for every effective voxel configuration. The efficiency of Class 9 can be improved by dividing it into two subcases: (1) all edge-adjacent (i.e., 18-adjacent but not 6-adjacent) neighbors are marrow, in which case, $\eta(p) = \delta(p) = 0$ and $\xi(p)$ equals the number of bone voxels in $N^*(p)$. (2) At least one edge-adjacent neighbor is bone, in which case the number of effective voxels is 17. Note that the two vertex-adjacent (i.e., 26-adjacent but not 18-adjacent) neighbors on the dead edge are no longer effective and that the configuration of the bone edge neighbor is already known. At this stage, one can use a precomputed lookup table for $\xi(p)$ and $\eta(p)$; note that for Class 9, $\delta(p)$ is always zero. This step reduces the size of a lookup table by a factor of 8.

III. TOPOLOGICAL CLASSIFICATION

The objective of topological classification is to uniquely determine the topological class of each voxel in a surface representation of the 3D network. Let us first explain the idea in continuous 3-space \mathcal{R}^3 . Let $S_{\mathcal{R}}$ be the union of a finite number of surfaces and curves, each with a finite area or length in \mathcal{R}^3 (Fig. 5a). It is interesting to note that a point in $S_{\mathcal{R}}$ can be classified depending on its local topological property in $S_{\mathcal{R}}$. For example, in a sufficiently small neighborhood of a point, p_s , on a surface, removal of p_s always creates a tunnel. For a point, p_{ss} , on a junction of surfaces, it creates multiple tunnels. It

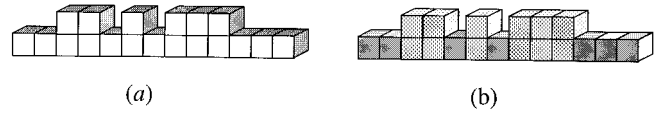


Figure 6. (a) Example of a structure resulting in profile elements. (b) Classification of profile elements (shown by dotted voxels); all others voxels are classified as curve elements.

creates exactly two objects for a point like p_c on a curve and multiple objects for a point like p_{cc} at the junction of curves. At a junction of surface and curve, like p_{sc} , it creates multiple objects and one tunnel. However, the classification is not so straightforward in a digital space.

The classes determined by classical digital topological analysis (Saha and Chaudhuri, 1996) are isolated voxels (*I*-type), curve interiors (*C*-type), curve edges (*CE*-type), curve-curve junctions (*CC*-type), surface interiors (*S*-type), surface edges (*SE*-type), surface-surface junctions (*SS*-type), and surface-curve junctions (*SC*-type; Fig. 5b). To these classes, we have introduced the concept of profile elements (*P*-type). These profiles are flat, ribbonlike structures that lead to a topological classification as surface edges with no adjacent surface interiors (Fig. 6). The method for detecting these profile elements is described at the end of this section.

After $\xi(p)$, $\eta(p)$, and $\delta(p)$ have been determined for each voxel in a surface representation of the trabecular network, we can proceed to the three-step topological classification. Taking a three-step approach makes the method simpler to understand and more efficient to implement. Furthermore, the classification is divided into three distinct steps because the local topological parameters of a single voxel in some cases cannot uniquely determine the topological class. For example, given the two surface representations in Figure 7, the local topological parameters of p in Figures 7(a) and (c) are identical (when p is considered as marrow): one object, one tunnel, and no cavities (ξ, η, δ). However, in Figure 7(a), p is a surface element and in Figure 7(c), p is a junction of two curves. The unique classification of p can be determined by looking at the parameters of the neighboring voxels to p . The neighbors of p in Figure 7(a) have $(\xi, \eta, \delta) = (1, 1, 0)$, whereas those in Figure 7(c) have $(\xi, \eta, \delta) = (2, 0, 0)$.

The three steps of topological classification are (1) determination of the local topological type, (2) the initial classification based on these types, and (3) the final classification to detect some junction cases and profiles. The first step determines the initial topological type (Table I), which, as demonstrated above, cannot always uniquely determine the topological class. More specifically, T_1, T_3, T_4 give unique initial voxel classifications, whereas T_2, T_5, T_6, T_7 ,

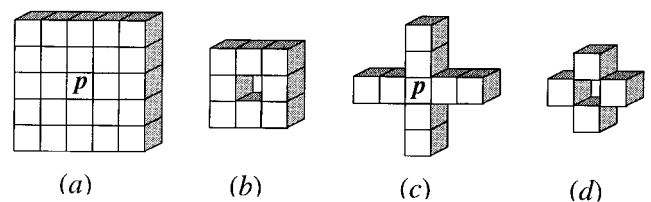


Figure 7. Examples where local topological parameters fail to uniquely classify different architectures. Local topological parameters of p in both (a) and (c) are the same. Excluded neighborhood of p in (a) and in (c) are shown in (b) and (d), respectively.

Table I. Initial decision table for bone voxel classification.

$\xi(p)$	$\eta(p)$	$\delta(p)$	Initial Type	Possible Initial Classification
0	0	0	T_1	<i>I</i> -type
1	0	0	T_2	<i>SE</i> -type or <i>CE</i> -type
2	0	0	T_3	<i>C</i> -type
>2	0	0	T_4	<i>CC</i> -type
1	1	0	T_5	<i>S</i> -type or <i>CC</i> -type
>1	≥ 1	0	T_6	<i>S</i> -type, <i>SC</i> -type or <i>CC</i> -type
1	>1	0	T_7	<i>S</i> -type, <i>SC</i> -type or <i>CC</i> -type
1	0	1	T_6	<i>S</i> -type, <i>SC</i> -type or <i>CC</i> -type

T_8 give two or more initial voxel classifications. During the second step, we review the 26-neighborhood of any voxel not uniquely classified by Table I and use Table II for the initial classification.

After the initial classification, the process is complete except for determination of profile elements and possible corrections at some surface junctions (Figs. 6, 8, and 9).

Figure 8 illustrates the problem of extension of *SS*-lines (a 26-path of *SS*-type voxels). In Figures 8(a) and 8(b), the *SS*-line should be extended to reach the surface edges as shown in Figures 8(c) and 8(d), respectively. Care must be taken in extending *SS*-lines. This is because in another example (Fig. 10), the *SS*-line should not be extended at the ends. In Figure 9, the curve is 26-connected to the surface, but the junction voxel has not been classified as *SC*-type.

A. Extension of *SS*-Lines. To find extensions to *SS*-lines, we must look at the topology of surface edges around the end-points of the *SS*-lines. Ideally, a surface edge forms a simple closed curve when there is no surface-surface junction; otherwise, this closed curve will be broken by the *SS*-line. Because the first two classification steps might not detect the end-points of these *SS*-lines, these points will be classified as *SE*-types. If any of the *SE*-type voxels near the end-points of *SS*-lines form junctions between *SE*-lines (Fig. 8a), or are end-points of *SE*-lines (Fig. 8b) but have not been classified correctly, they are changed to *SS*-type voxels. The following definitions and algorithm will find these misclassified voxels. Let S_{SE} denote the set of all *SE*-type voxels in the surface representation. Let p be an end voxel of an *SS*-line (an end voxel has at most one 26-adjacent *SS*-type voxel). The single *SS*-type voxel in $N^*(p)$ will

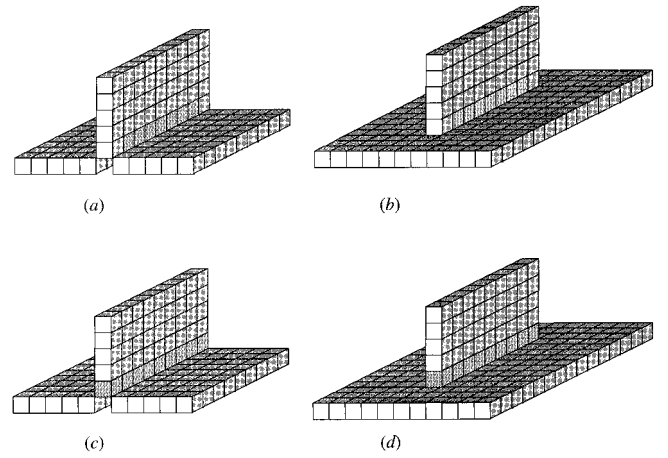


Figure 8. Extension of *SS*-lines (*SS*-type voxels are shown by dotted voxels): (a), (b) The *SS*-line obtained using Tables I and II. (c), (d) The *SS*-line after the extension process.

be denoted p_{ss} , and let P_S denote the set of all *S*-type voxels in $N^*(p)$.

for every *SE*-type voxel $q \in N^*(p) - N^*(p_{ss})$ we evaluate the following algorithm:

if $S_{SE} \cap N^*(q)$ contains more than two 26-objects OR forms tunnels then

flag q ;

else if $S_{SE} \cap N^*(q)$ contains exactly one 26-object

AND $\exists r \in P_S \cap N^*(q) - N^*(p_{ss})$ s.t. $|q - r| < |q - p|$

then

flag one of the r 's nearest to q ;

Note that after the last “then” statement, the flagged voxel is not q but one (there might be several) of the voxels closest to q in $P_S \cap N^*(q) - N^*(p_{ss})$. All flagged voxels are reclassified as *SS*-type voxels. If the algorithm is executed on Figures 8(a) and (b), we obtain Figures 8(c) and (d), respectively.

B. Finding Junctions Between Curves and Surfaces. If a curve voxel is adjacent to a surface, there must be a junction in between them. Because some of these surface-curve junctions will not be detected after the second step of classification, we must look at all surface voxels that are neighbors of a curve voxel and find if a surface-curve junction is needed. The algorithm is as follows: Let p be a *C*-type or *CC*-type voxel and let P be the set of *S*-type, *SC*-type, and *SS*-type voxels in $N^*(p)$. Let P_1, P_2, \dots, P_n be the 26-objects in P . If P_i has no *SC*-type or *SS*-type voxel, the nearest

Table II. Initial decision table for bone voxel classification.

Initial Type	Neighborhood Analysis	Initial Classification
T_2	Exactly one bone neighbor	<i>CE</i> -type
T_2	More than one bone neighbor	<i>SE</i> -type
T_5	All bone neighbors are T_3 or T_4	<i>CC</i> -type
T_5	Not all bone neighbors are T_3 or T_4	<i>S</i> -type
T_6	All bone neighbors are T_3 or T_4	<i>CC</i> -type
T_6	Some (not all) bone neighbors are T_3 or T_4	<i>SC</i> -type
T_6	No bone neighbor is T_3 or T_4	<i>CC</i> -type
T_7	All bone neighbors are T_3 or T_4	<i>CC</i> -type
T_7	Some (not all) bone neighbors are T_3 or T_4	<i>SC</i> -type
T_7	No bone neighbor is T_3 or T_4	<i>CC</i> -type
T_8	All bone neighbors are T_3 or T_4	<i>CC</i> -type
T_8	Some (not all) bone neighbors are T_3 or T_4	<i>SC</i> -type
T_8	No bone neighbor is T_3 or T_4	<i>CC</i> -type

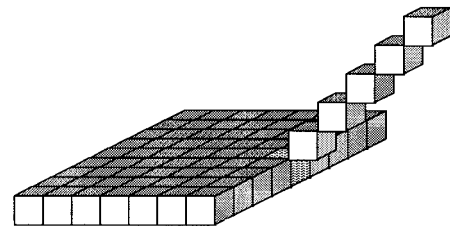


Figure 9. The *SC*-type voxel (shown by dotted cube) cannot be detected using Tables I and II.

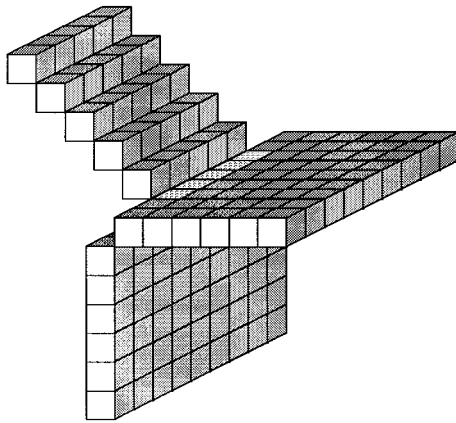


Figure 10. An example where the extension of SS-line (SS-type voxels are shown by dotted voxels) at two ends is not needed.

voxel to p in P_i is reclassified as an SC -type voxel. The SC -type junction voxel of Figure 9 is detected by this algorithm.

C. Profile Elements. One major structural type missing from classical digital topology is the concept of a profile-type element. Because rodlike biological structures are rarely perfect cylinders, and the thresholding process of partial BVF voxels will produce further cross-sectional distortions, our resulting surface skeleton representation may have curves that consist of two-voxel width surfaces (Fig. 6). The resulting topological analysis classifies these curves as double rows of surface edges. Because it would be more accurate to describe these profiles as curves, we have developed a method to identify profiles and label them accordingly. Because a surface edge, by definition, must be adjacent to a surface, any surface edge that is not should be classified as a profile. The following is the formal definition of profiles: A profile-type (P -type) voxel is any SE -type voxel, p , with no S -type, SC -type, or SS -type voxels in $N^*(p)$. In voxel counting, two P -type voxels will be counted as one C -type voxel. P -type voxels will always appear in pairs across the curve direction because a single voxel would have been classified as a curve point.

IV. METHODS

The data sets used in this study consisted of three types, each demonstrating and validating a different aspect of the method: synthetically generated images and MR images of human trabecular bone from the distal radius in cadaveric specimens and *in vivo*. Synthetic data were generated to evaluate the accuracy of the method. To visually confirm the trabecular bone morphology (plate likeness vs. rod likeness) predicted by topological parameters, images acquired in conjunction with an earlier project (Hwang et al., 1997) were reexamined. These high-resolution images of cadaveric specimens had isotropic voxel size of $78 \times 78 \times 78 \mu\text{m}^3$, which preserves 3D trabecular micro-architecture. It was shown that structural parameters derived from these images are predictive of Young's modulus for uniaxial loading. Finally, selected *in vivo* images from patients representing varying skeletal status in terms of their morphology and age, but of similar BVF and bone mineral density estimates, were examined.

A. Synthetic Images. IDL (RSI Inc., Boulder, CO) was used to generate synthetic images of idealized trabecular networks using

cubic spline surfaces and curves. Rodlike and platelike structures were generated through semiregular grid points, with uniform random variations in position, similar to those seen *in vivo*. Plate location varied by up to five pixels normal to the plate, rod location by up to three pixels in each of two transverse dimensions to the rod axis.

The voxel size of *in vivo* MR images is typically of the same order of magnitude as the trabecular thickness, so mimicking the partial volume effect was important in generating the synthetic images. A numerical method was used to generate binary rods and plates, with an exact structure thickness. The resolution was then reduced to simulate this partial volume effect. For example, if a plate thickness of 1.3 was desired with a precision of 0.1, an initial image was generated with a thickness of 13 voxels. This initial image was then resampled to reduce the resolution by a factor of 10 as a means to simulate the partial volume blurring effect resulting from the limited resolution achievable *in vivo*. In this case, each voxel represents the fractional volume occupancy of bone (BVF) for that voxel in the digital space. The method resulted in wavy plates of thickness ranging from 0.6 to 1.6 voxels (Fig. 11), and rods ranging in diameter from 0.6 to 1.6 voxels. Groups of plates and rods with the same thickness were combined using geometric partial volume considerations at the intersections to produce the complex synthetic images. The plate images consisted of five individual plates along both the x and y directions for a total of 10 intersecting plates in the image (5×5 pattern; Fig. 11). The rod images consisted of 100 rods along the x dimension (in a 10×10 pattern spaced evenly along y and z) intersecting a perpendicular reference plate.

Rician noise (Gudbjartsson and Patz, 1995) comparable to *in vivo* images was added to all synthetic images to simulate the noise characteristics of magnitude *in vivo* MR images. The images were analyzed using the methods presented here. These synthetic images contained known counts of surface and curve voxels and the results of the topological analysis were compared with these known quantities to evaluate the absolute accuracy of the method. Because current *in vivo* MRI resolution is on the order of the trabecular thickness, accuracy of the topological parameters as a function of structure resolution is of particular interest. Toward this goal, the surface and curve count accuracy was plotted as a function of plate thickness and curve diameter.

B. Trabecular Bone Images. Images from a prior study (Hwang et al., 1997) were used to confirm the visually observed differences between platelike and rodlike trabecular bone networks. These specimens were obtained from 9-mm cores of trabecular bone from the human radius acquired at $78 \times 78 \times 78 \mu\text{m}^3$ resolution. Images were chosen that qualitatively display more rodlike vs. more

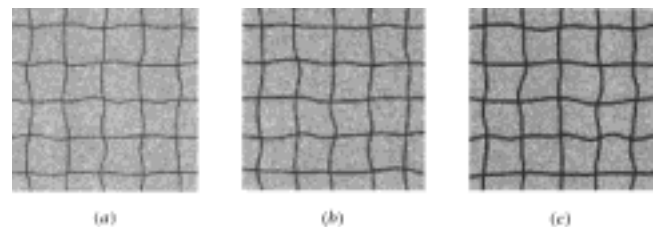


Figure 11. Examples of synthetic images used to evaluate the absolute accuracy of topological analysis. The 3D data set is filled with a $5 \times 5 \times 5$ grid of wavy plates at varying voxel thicknesses. Pictured are (a) 0.6, (b) 1.1, and (c) 1.6-voxel thick plate arrays.

Table III. Results of synthetic image analysis showing absolute accuracy of the topological analysis method as a function of structure size.

Curve Diameter ^a	Accuracy %	St. Dev. %	Surface Thickness ^a	Accuracy %	St. Dev. %
0.6	51.0	0.61	0.6	98.0	0.049
0.7	50.6	0.81	0.7	98.4	0.035
0.8	85.1	0.15	0.8	98.4	0.084
0.9	90.2	0.16	0.9	98.2	0.030
1.0	96.6	0.08	1.0	98.2	0.085
1.1	97.2	0.11	1.1	98.0	0.039
1.2	97.7	0.04	1.2	98.0	0.111
1.3	97.5	0.07	1.3	98.3	0.054
1.4	97.6	0.07	1.4	98.8	0.181
1.5	97.7	0.04	1.5	98.7	0.011
1.6	98.5	0.20	1.6	98.6	0.118

^a Voxel units.

platelike morphologies. *In vivo* images were acquired as part of an ongoing clinical study to evaluate the architectural differences occurring in osteoporosis. For each subject, 28 slices were acquired ($512 \times 256 \times 28$ matrix size, $137 \times 137 \mu\text{m}$ inplane resolution, 350-mm slice thickness, radiofrequency pulse flip angle = 140° , TR = 80 ms, TE = 3D 9.7 ms). In addition, the pulse sequence was equipped with navigator echoes to correct for translational motion of the wrist during scanning, as described in Song and Wehrli (1999). Three high-resolution *in vivo* images of nonosteoporotic subjects of varying age were analyzed topologically and the results were compared both visually and numerically.

C. Preprocessing. The MR images were preprocessed by shading and noise reduction using a histogram deconvolution method (Hwang and Wehrli, in press). The resulting image represents the BVF for each voxel. The volume of interest (VOI) was manually outlined for each slice and adjusted to exclude areas of high noise or acquisition artifacts. The *in vivo* image resolution was enhanced using a subvoxel classification technique similar to the one described by Wu et al. (1994), resulting in a final voxel size of $68 \times 68 \times 88 \mu\text{m}$.³ In this manner, an in-slice and across-slice continuity of the trabecular network was achieved, which aided preservation of topology during the skeletonization procedure. Projection images from a cylindrical VOI taken from the geometric center of the distal radius were displayed, representing virtual bone biopsies.

D. Thresholding and Skeletonization. Topological parameters require a surface representation of the binarized trabecular bone network. There can be no bulk elements present in the digital image. Also, all volume objects must be reduced to 1D or 2D structures, which was accomplished by thresholding and skeletonizing. Toward this goal, a BVF threshold of 0.25 was used for all images. The threshold was selected because it gives the minimum change in skeleton count and represents the minimum change in partially volumed structures. After thresholding, the binarized images were skeletonized to reduce the dimensionality of the trabecular bone network structure, i.e., plates become surfaces and rods become curves or profiles. We implemented a recently published skeletonization algorithm (Saha et al., 1997) because of its robustness to noise and rotation.

E. Topological Classification and Analyses. After conversion to a skeletonized surface representation, local topologies were determined for the images as described above. However, the results of this classification had to be further evaluated to account for VOI

edge artifacts, normalization of different resolutions, and different sample sizes. To remove the edge artifact caused by analyzing a VOI, the VOI was eroded before voxel classification type counting. Edge artifacts result from two processes: the creation of artificial edges in the trabecular structure caused by the VOI boundaries and from the skeletonization process on these edges. During each iteration of the skeletonization process, the VOI edge artifact propagates no more than one voxel layer into the structure. Therefore, for skeletonization proceeding through n iterations, a cubic erosion mask of size $2n + 1$ was needed. In this manner, edge artifacts caused by the skeletonization and classification processes were eliminated.

To reduce the complexity of the data analysis, classification counts of the similar type elements were combined. The surface edge and surface interior voxels were counted together as surface voxels; similarly, both the edge and interior voxels of curves were counted as curve voxels. One half of the profile voxel counts was added to the curve counts. Finally, all the different types of junction voxels were counted as junction voxels. The result of this operation is four different categories of voxels: isolated, curve, surface, and junction voxels. Finally, the classification counts were normalized to the VOI volume, resulting in parameter densities.

V. RESULTS AND DISCUSSION

The data in Table III show that for rodlike structures (i.e., curves) of greater than 0.9-voxel diameter, the method is capable of correctly classifying voxels as belonging to curves with an accuracy of 97%. However, accuracy decreases rapidly at lower resolution. The classification errors at lower resolution are caused by increasing partial volume blurring. For rods of 0.6 and 0.7-voxel diameters, the voxels are only partially occupied by “bone” (0.07–0.28 and 0.095–0.38, respectively), depending on how many voxels the curve intersects. These BVF values and our choice of threshold at 0.25 BVF caused many of the rod voxels to disappear. At higher curve diameters, BVF increased sufficiently for more elements to survive after thresholding, resulting in increased classification accuracy. Lowering the threshold would include more curve points for low BVF images, but would also cause misclassification due to noise.

For plates (surfaces), the accuracy was found to be greater than 98% for all plate thicknesses tested (Table III). This result is consistent with our findings for the rod images: the choice of threshold and the partial volume effect is key in determining the structural elements that will survive the skeletonization. At a plate thickness of 0.6-voxel units, the minimum BVF at any plate location will be 0.3 (when the plate is equally distributed across two voxels).

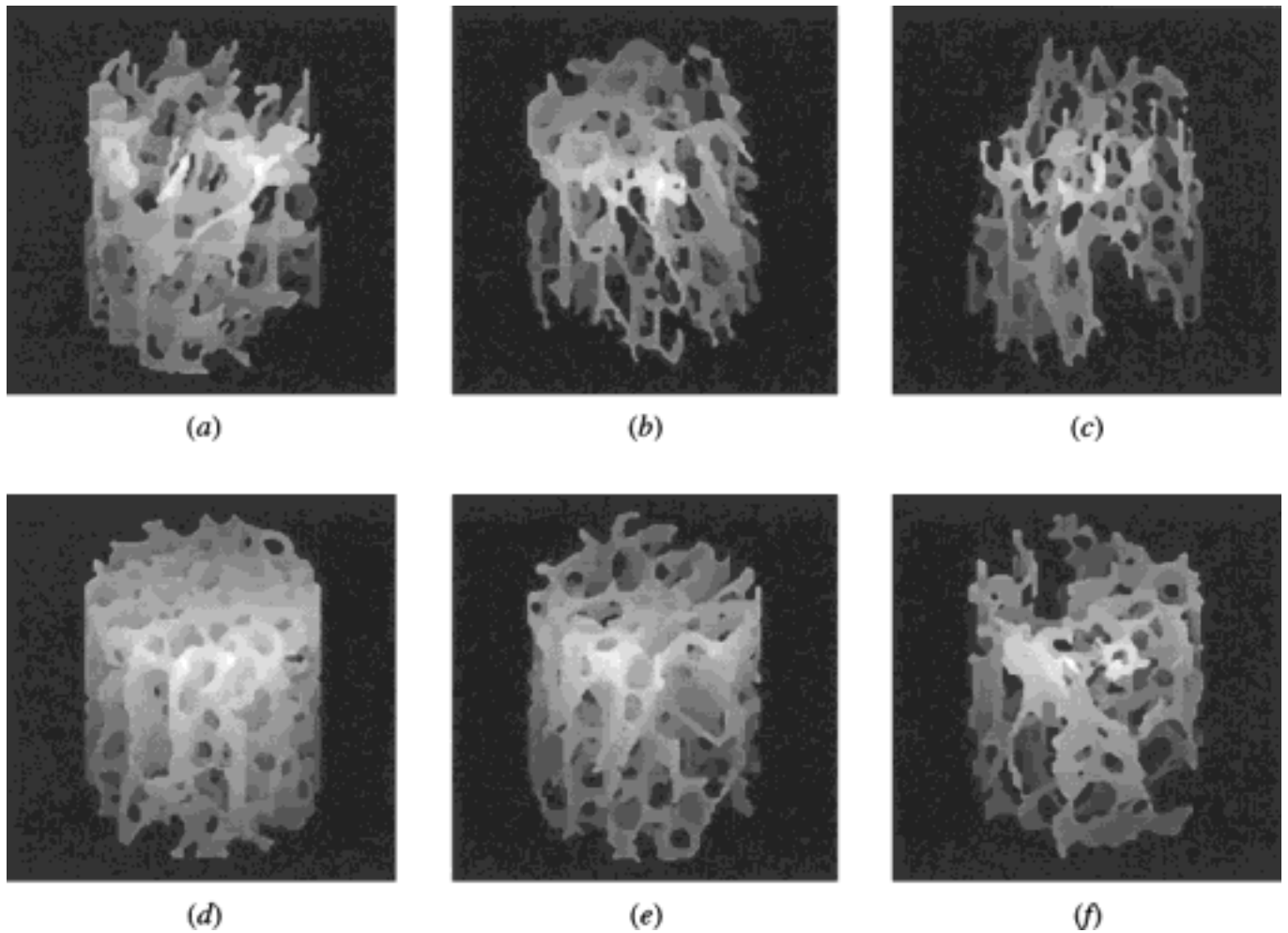


Figure 12. Qualitative comparison of topological parameters with platelike and rodlike appearing morphologies of trabecular networks. (a)–(c) Projection images ($78 \times 78 \times 78 \mu\text{m}^3$) of specimens from the distal radius in three female subjects, ages 53, 74, and 87 years, respectively. Images from three male subjects, ages 80 (d) and (e) and 78 years (f). In both rows, plate likeness decreases whereas rod likeness increases from left to right. Note the highly intact predominantly platelike architecture of the bone in the 80-year-old subject (d). The estimated topological parameters in Table IV emphasize the interindividual differences.

Therefore, a choice of 0.25 as the BVF threshold should include all partially occupied plate voxels. These results suggest that most plate and rod voxels can be identified *in vivo*, and that plate counts will be more accurate than rod counts at current *in vivo* resolutions.

The projection images of the *in vitro* data (Fig. 12) show six specimens from subjects of varying age, gender, and BVF (Table IV). The changes in morphology can be readily visualized in these images, which demonstrate increasing erosion from left to right. The

top row shows how trabecular networks change to become more rodlike with increasing age among three postmenopausal women. The surface-curve ratio and erosion index underscore these differences. The bottom row images are from three male donors of nearly equal age. The images demonstrate dramatic differences in trabecular topology, with a highly intact network of plates in Figure 12(d) and, to a lesser extent in Figure 12(e), but a more eroded structure in Figure 12(f). Again, the surface-curve ratio and the erosion index exacerbate the trend.

Table IV. Estimated topological parameters of six *in vitro* data sets from six specimens of human trabecular bone shown in Figure 12.

Figure	Sex	Age	BVF	Surface/Curve	Erosion Index
(a)	F	53	0.120	19.8	0.643
(b)	F	74	0.116	13.8	0.870
(c)	F	87	0.078	5.81	1.100
(d)	M	80	0.189	43.3	0.270
(e)	M	80	0.152	26.9	0.387
(f)	M	78	0.099	14.8	0.612

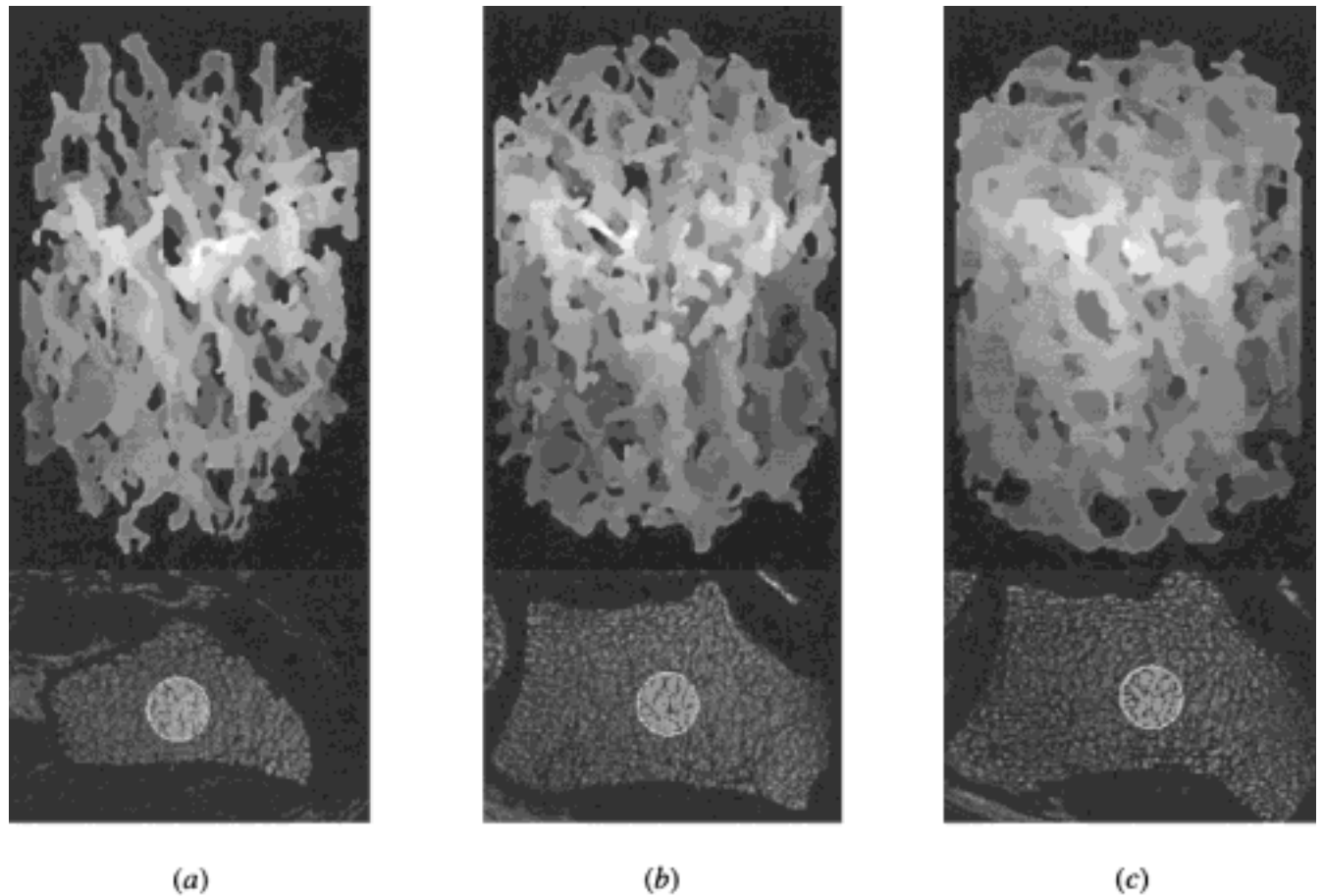


Figure 13. *In vivo* MR projection images of cancellous bone from the metaphysics of the human radius at $137 \times 137 \times 350 \mu\text{m}^3$ demonstrating varying morphology: (a) 73-year-old woman with osteopenia (reduced vertebral bone density), (b) 49-year-old woman of normal bone mineral density, and (c) a 30-year-old man. Topological parameters indicate increasing surface and decreasing curve densities from (a) to (c). Surface-to-curve ratios are 5.9, 7.2, and 11.9 for (a), (b), and (c), respectively; erosion indices are 1.22, 1.07, and 0.72.

The trend seen in the *in vitro* study can be further exemplified by a series of *in vivo* examples. Figure 13 shows three subjects of varying age and correspondingly different architectures. The images in Figure 13(a) display both numerically and visually a strong rodlike architecture unlike those in Figure 13(c), which are predominantly platelike. These differences in morphology can be understood considering that the images in Figure 13(a) are from a 73-year old woman; those in Figure 13(c) are from a 30-year-old man; and those in Figure 13(b), which display a mixed architecture of plates and rods, are from a 49-year-old woman. The topological parameters parallel the same trend seen visually with surface-curve ratios of 5.9, 7.2, and 11.9 and erosion indices of 1.22, 1.07, and 0.72. The cross-sections below the projections show that the cylindrical cores were taken from the same relative location despite the obviously different morphologies.

VI. CONCLUSIONS

In this work, the potential of digital topology as a means to quantitatively characterize the 3D architecture of cancellous bone networks is demonstrated. An important property of the proposed method is its ability to uniquely classify each bone voxel after binarization and skeletonization, therefore providing local connectivity information. The known conversion of plates to rods during

normal aging, especially in osteoporosis, may be followed quantitatively by measuring the surface-curve ratio, or an erosion index, as composite parameters directly amenable from the analysis. The dramatic variations in cancellous bone morphology occurring among subjects of different age and disease state are illustrated with virtual bone biopsies derived from *in vivo* MR micro images. Finally, because the mechanical properties of cancellous bone networks are highly dependent on their structural organization, the method may be suited for strength assessment *in vitro* and prediction of fracture risk *in vivo*.

ACKNOWLEDGMENTS

The authors are grateful to Dr. S.N. Hwang for providing a program for subvoxel tissue classification prior to publication, and to Dr. H.K. Song for helpful discussions.

REFERENCES

- M. Amling, M. Posl, H. Ritzel, M. Hahn, M. Vogel, V.J. Wening, and G. Delling, Architecture and distribution of cancellous bone yield vertebral fracture clues: A histomorphometric analysis of the complete spinal column from 40 autopsy specimens, *Arch Orthop Trauma Surg* 115 (1996), 262–269.
- R.T. deHoff, E.H. Aigeltinger, and K.R. Craig, Experimental determination of the topological properties of three-dimensional microstructures, *J Microsc* 95 (1972), 69–91.

- L.A. Feldkamp, S.A. Goldstein, A.M. Parfitt, G. Jesion, and M. Kleerekoper, The direct examination of three-dimensional bone architecture *in vitro* by computed tomography, *J Bone Miner Res* 4 (1989), 3–11.
- C.L. Gordon, C.E. Webber, J.D. Adachi, and N. Christoforou, *In vivo* assessment of trabecular bone structure at the distal radius from high-resolution computed tomography images, *Phys Med Biol* 41 (1996), 495–508.
- C.L. Gordon, C.E. Webber, N. Christoforou, and C. Nahmias, *In vivo* assessment of trabecular bone structure at the distal radius from high-resolution magnetic resonance images, *Med Phys* 24 (1997), 585–593.
- H. Gudbjartsson and S. Patz, The Rician distribution of noisy MRI data, *Magn Reson Med* 34 (1995), 910–914.
- S.N. Hwang and F.W. Wehrli, Estimating voxel volume fractions of trabecular bone on the basis of magnetic resonance images acquired *in vivo*, *Int J Imaging Syst Technol* 10 (1999), 186–198.
- S.N. Hwang and F.W. Wehrli, Estimating voxel volume fractions of trabecular bone on the basis of magnetic resonance images acquired *in vivo*, *Int J Imaging Syst Technol* (in press).
- S.N. Hwang, F.W. Wehrli, and J.L. Williams, Probability-based structural parameters from three-dimensional nuclear magnetic resonance images as predictors of trabecular bone strength, *Med Phys* 24 (1997), 1255–1261.
- J.H. Kinney and A.J. Ladd, The relationship between three-dimensional connectivity and the elastic properties of trabecular bone, *J Bone Miner Res* 13 (1998), 839–845.
- T.Y. Kong and A. Rosenfeld, Digital topology: Introduction and survey, *Computer Vision Graphics Image Process* 48 (1989), 357–393.
- R. Müller, T. Hildebrand, and P. Rüeggsegger, Noninvasive bone biopsy: A new method to analyse and display the three-dimensional structure of trabecular bone, *Phys Med Biol* 39 (1994), 145–164.
- A.M. Parfitt, “Stereologic basis of bone histomorphometry: Theory of quantitative microscopy and reconstruction of the third dimension,” *Bone Histomorphometry: Techniques and interpretation*, R.R. Recker (Editor), CRC Press, Boca Raton, FL 1981, pp. 53–87.
- A.M. Parfitt, Implications of architecture for the pathogenesis and prevention of vertebral fracture, *Bone* 13 (1992), S41–S47.
- A. Rosenfeld, Adjacency in digital pictures, *Inform Control* 26 (1974), 24–33.
- P.K. Saha and B.B. Chaudhuri, 3D digital topology under binary transformation with applications, *Computer Vision Image Understand* 63 (1996), 418–429.
- P.K. Saha, B.B. Chaudhuri, and D. Duuta Majumder, A new shape preserving parallel thinning algorithm for 3D digital images, *Pattern Recogn* 30 (1997), 1939–1955.
- P.K. Saha and A. Rosenfeld, Strongly normals sets of convex polygons or polyhedra, *Pattern Recogn Lett* 9 (1998), 1119–1124.
- P.K. Saha and A. Rosenfeld, Determining simplicity and computing topological change in strongly normals partial tilings of R^2 and R^3 , *Pattern Recogn* 33 (2000), 105–118.
- H.K. Song and F.W. Wehrli, *In vivo* micro-imaging using alternating navigator echoes with applications to cancellous bone structural analysis, *Magn Reson Med* 41 (1999), 947–953.
- F.W. Wehrli, S.N. Hwang, and H.K. Song, New architectural parameters derived from micro-MRI for the prediction of trabecular bone strength, *Technique Health Care* 6 (1998), 307–320.
- World Health Organization, Assessment of fracture risk and its application to screening for postmenopausal osteoporosis, WHO Technical Report Series, World Health Organization, Geneva, 1994, p. 4.
- Z. Wu, H. Chung, and F.W. Wehrli, A Bayesian approach to subvoxel tissue classification in NMR microscopic images of trabecular bone, *Magn Reson Med* 31 (1994), 302–308.